Key Points:
- We studied the parallel electrical conductivity in the topside ionosphere at high magnetic latitudes by using 4-year measurements acquired by the Swarm mission
- We investigated both the climatological properties and the seasonal variations of electrical conductivity
- By comparing the results obtained with the International Reference Ionosphere model we estimated the contribution to electrical conductivity mainly due to particle precipitation

Correspondence to:
F. Giannattasio,
fabio.giannattasio@ingv.it

Parallel Electrical Conductivity in the Topside Ionosphere Derived From Swarm Measurements

F. Giannattasio[1] , **P. De Michelis**[1] , **A. Pignalberi**[1] , **I. Coco**[1] , **G. Consolini**[2] ,
M. Pezzopane[1] , **and R. Tozzi**[1]

[1]Istituto Nazionale di Geofisica e Vulcanologia, Roma, Italy, [2]INAF - Istituto di Astrofisica e Planetologia Spaziali, Roma, Italy

Abstract Our knowledge of the physical properties of the topside ionosphere is still incomplete. A key point still not fully understood is how field-aligned currents are generated, evolve and dissipate in the ionosphere. Answering to this question is fundamental for a better understanding of the mechanisms regulating the coupling between magnetosphere and ionosphere and to shed light on the physical processes inherent to space weather events occurring in the Earth's ionosphere. In this framework a relevant role is played by the ionospheric conductivity. The purpose of this study is to analyze the main properties of the electrical conductivity parallel to the geomagnetic field from a climatological point of view. The statistical study of the electrical conductivity is proposed using four years of in-situ electron density and temperature measurements at 1 Hz acquired by the European Space Agency's Swarm A satellite. Variations due to seasonal effects are also investigated. Finally, starting from observations and comparing our results with those obtained using International Reference Ionosphere model, we give a first estimation of the conductivity mainly due to particle precipitation.

1. Introduction

The study of the spatial and temporal structure of high-latitude ionospheric current systems is of utmost importance for both the improvement of magnetosphere-ionosphere coupling models and for practical purposes. The ionospheric current systems can lead to a variety of important space weather effects, influencing the performance of space-born and ground-based systems. For example, ground-based systems may be subject to peaky induced geoelectric fields and associated currents (Boteler & Pirjola, 2017; Boteler et al., 1998). On the other hand, geomagnetic field disturbances caused by strong ionospheric currents may affect the positioning and navigation systems (Poedjono et al., 2013). The intensification of plasma streams may also contribute to increase the atmospheric drag acting on low-Earth-orbit satellites, thus resulting in the lowering of the flight altitude (Liu & Lühr, 2005; Pirjola et al., 2005). For these reasons, in-situ measurements of physical parameters characterizing the ionospheric F-layer are fundamental. They are aimed at significantly improving our understanding of space weather phenomena and their impact on Earth, especially at high latitudes, where effects of solar wind-magnetosphere-ionosphere coupling can be captured, such as, e.g., the precipitation of solar plasma, the intensification of ionospheric currents, together with the effects of dynamic processes occurring in the geomagnetic tail regions (Cowley et al., 2003; Hones, 1979; Horton et al., 1999; Kamide & Baumjohann, 1993; Lyon, 2000; Milan et al., 2017; Song et al., 2005; Stumpo et al., 2020).

At high magnetic latitudes the ionospheric current system consists of both horizontal and vertical currents. The former flow in the ionospheric E-layer between ~90 and ~110 km of altitude and divide into mutually orthogonal Hall and Pedersen currents (Amm, 1997; Kamide & Baumjohann, 1993). The latter are the so-called field-aligned currents (FACs), which are often referred to as Birkeland currents in honor of the man who proposed them for the first time in the early 1900s before their detection by Zmuda et al. (1966). FACs are known to be responsible for the coupling between the solar wind-magnetosphere system and the ionosphere. This coupling manifests in the dayside as, for example, a direct precipitation of solar particles (mainly electrons, protons, and alpha particles) in conditions of open magnetosphere; and in the nightside as, for example, plasma acceleration in response to substorm events involving magnetospheric convection occurring far away in the magnetotail. The large-scale distribution of currents at high latitudes results in three main systems (Iijima & Potemra, 1978; Zmuda & Armstrong, 1974): (1) a more poleward current

sheet called Region 1 (R1), which flows toward the magnetosphere in the evening sector and toward the ionosphere in the morning sector; (2) a more equatorward current sheet called Region 2 (R2), which flows in the opposite direction, i.e., toward the ionosphere in the evening sector and toward the magnetosphere in the morning sector. Both R1 and R2 overlap in the premidnight Harang region (Harang, 1946); and (3) the zonal electrojets flowing along the auroral oval in the night sector and the Pedersen currents flowing across the auroral oval (Boström, 1964), both connecting FACs flowing in opposite directions. However, despite Hall and Pedersen currents also contribute to the energy of the high-latitude ionosphere and respond to the chain of dynamic processes due to the solar wind-magnetosphere-ionosphere coupling, they are confined in a rather thin layer of the ionosphere, reaching their maximum intensity at altitudes between 90 and 110 km. At higher altitudes their contribution is expected to quickly become negligible (Brekke & Hall, 1988; de la Beaujardiere et al., 1991; Moen & Brekke, 1993; Rasmussen et al., 1988). Thus, FACs are responsible for the exchange of most of plasma energy and momentum with the magnetosphere.

A physical parameter that is, fundamental to characterize the ionospheric currents features i.e., their magnitude, spatial distribution and temporal variations, is the electrical conductivity. In fact, due to the Ohm's law, it provides both the link between the onset of an electric field and the amplification of currents, and the rate of dissipation of currents in a medium via Joule heating, i.e., the power per unit volume dissipated in a resistive plasma. Over the years, several techniques have been developed that take advantage of measurements of the magnetic disturbance field to estimate the ionospheric equivalent current systems responsible for the disturbance. Interesting results have been obtained capable of reproducing the horizontal and FACs via sophisticated models of electrical conductivity (Kamide et al., 1981; Pulkkinen et al., 2003; Weygand et al., 2011). Of course, for this reason results were strictly dependent on the model used for conductivity. Average conductivity models dependent on latitude, local time, and different levels of geomagnetic disturbance were developed by using satellite measurements of electron precipitation (Spiro et al., 1982). Nevertheless, these measurements were not able to capture those spatiotemporal variations that are typical of ionospheric conductivity during the development of geomagnetic substorms. Incoherent scatter radar measurements can be used to provide electron density and ionospheric conductivity (Robinson et al., 1985a, 1985b), but they suffer from low spatial and temporal resolutions, preventing them from being related to fast dynamic phenomena like, e.g., substorms. Electron density can be still computed by the energy flux spectrum of the precipitating electrons, as done by using rocket and satellite measurements (Fuller-Rowell & Evans, 1987; Marklund et al., 1982). But, also in this case, none of these studies has provided the necessary spatiotemporal resolution to capture the fine structure of the high-latitude dynamic ionosphere during substorm and energetic events. Despite electron density profiles acquired by radar measurements were used to compute the ionospheric conductivities in the E-layer (Kirkwood et al., 1988), as well as ionosonde, radar scattering, balloons, rockets, and satellite data (Föpl et al., 1968; Germany et al., 1994; Holzworth et al., 1985; Mende et al., 1984; Mozer & Serlin, 1969), similar attempts to capture the properties of conductivity in the F-layer are still lacking or are poorly present. More recently, Amm et al. (2015) used Swarm measurements of the electric and magnetic field to infer, via a technique based on spherical elementary current systems (Amm, 1997), the field-aligned conductivity together with the Hall and Pedersen ones in the ionospheric current layer at ∼ 110 km of altitude. However, no study has directly provided high-resolution conductivity maps in the ionospheric F-layer by taking advantage of in-situ measurements.

The aim of this work is to study the field-aligned conductivity, which is the conductivity parallel to the Earth's magnetic field lines, in the topside ionosphere through in-situ measurements of electron density and temperature. To our knowledge, it is the first time that a climatological study is performed on parallel electrical conductivity, based on 4 years of uninterrupted data acquired by the Swarm A satellite. We built maps of parallel conductivity in quasi-dipole (QD) latitude versus magnetic local time (MLT) and put in evidence what are the characteristic features of electrical conductivity for both hemispheres and depending on season. We underline that in our study electrical conductivity is computed in the F-layer directly, based on high resolution measurements of electron density and temperature, and without resorting to models. Only a few reasonable assumptions were made on the electron density of the ionospheric plasma and on the collision rate between electrons, ions, and neutrals at Swarm altitudes.

The paper is organized as follows. In the next section we describe the data used and how we retrieved electrical conductivity; in §3 we show the results and discuss them in light of existing literature; in §4 we summarize the main steps and findings of this work and present the future perspective.

2. Data and Methods

2.1. Swarm Observations and Preliminary Analysis

We used 4 years of data acquired by the European Space Agency (ESA) Swarm A satellite (Friis-Christensen et al., 2006) from April 1, 2014 to March 31, 2018. During the selected period the satellite flew in a circular near-polar orbit at an average altitude of about 460 km and an orbit inclination plane of about 87.4°. Level 1b data, downloaded from the LATEST_BASELINES folder of the ESA dissemination server (ftp://swarm-diss.eo.esa.int), provided: UTC time, the position of the satellite in Earth-centered geographic coordinates, and in-situ electron density and temperature at 1 s cadence measured by the Langmuir probes, part of the electric field instrument (Knudsen et al., 2017) and filtered on the basis of quality flags provided by the mission team. In particular, according to the *Swarm Level 1b Product Definition* document, we excluded data flagged as "non nominal" (flags different from either 10 or 20). Data that were missing or not having passed the quality flags were replaced by NaN values in order to allow the continuity of the time series.

In order to study the nature of features due to the magnetosphere-ionosphere coupling, we used the non-orthogonal QD system of coordinates (Emmert et al., 2010; Laundal & Richmond, 2017; Richmond, 1995). The transformation to QD coordinates consists of two steps: first, a transformation from geocentric latitude, longitude, and satellite altitude to geodetic latitude, longitude, and altitude; second, the transformation from geodetic to QD coordinates (Emmert et al., 2010). The position of the Sun is taken into account by using MLT instead of UTC time.

The main features associated with the onset of FACs, namely the current sheets in Regions R1 and R2, have been identified by analyzing magnetic Level 1b data at low resolution (1 Hz) co-spatial and simultaneous with electric field instrument data, and according to the same quality flags. Magnetic data were processed with the last version of the CHAOS-6 package (Finlay et al., 2016), which models the geomagnetic field of internal origin at any satellite position. The subtraction of the modeled internal field from the observed field allowed us to obtain the observed geomagnetic field of external origin. Due to the Ampere law, in order to relate the variation of the vector magnetic field of external origin to the FACs flowing at Swarm A altitude, we computed the components of the external field in directions parallel and perpendicular to the main field, namely $\mathbf{B}_\parallel$ and $\mathbf{B}_\perp$. In fact, at high latitudes $\mathbf{B}_\perp$ can be thought as essentially originated by FACs, while $\mathbf{B}_\parallel$ as originated by horizontal currents.

In the top panel of Figure 1 we show the climatological maps of signed $\mathbf{B}_\perp$ for both the hemispheres. The sign is given by the sign of the West-East component. In fact, the orthonormal triad defining the directions of the vectors is such that inward FACs to the ionosphere have a positive West-East perpendicular component, while outward FACs from the ionosphere have a negative West-East perpendicular component. As we can see, Regions R1 and R2 are clearly visible, especially in the Southern Hemisphere (Milan et al., 2017). More in detail, in the Northern Hemisphere the equatorward edge of R2 is located between ∼ 60° and ∼ 65° QD latitude, and is characterized by positive $B_\perp$ (inward current) around dusk and negative $B_\perp$ (outward current) around dawn. On the other hand, the poleward edge of R1 is at ∼ 85° QD latitude, and is negative (outward current) around dusk and positive (inward current) around dawn. Opposite signs are found in the Southern Hemisphere in correspondence with R1 and R2 regions. In the bottom panel of the same figure we show the unsigned | $\mathbf{B}_\perp$ | as a function of the QD latitude for fixed MLTs. The different colors of the solid curves correspond to different MLTs. Curves have been smoothed by using a 4th-order Savitzky-Golay low-pass filter with a smoothing window's size of 17 points (Savitzky & Golay, 1964). With this representation, the regions affected by the current sheets associated with FACs correspond to the peaks at QD latitudes higher than ∼ 60° and at all MLTs. The features shown in Figure 1 are consistent with those found, e.g., in Iijima and Potemra (1978), which extension was found to depend on the geomagnetic activity level.
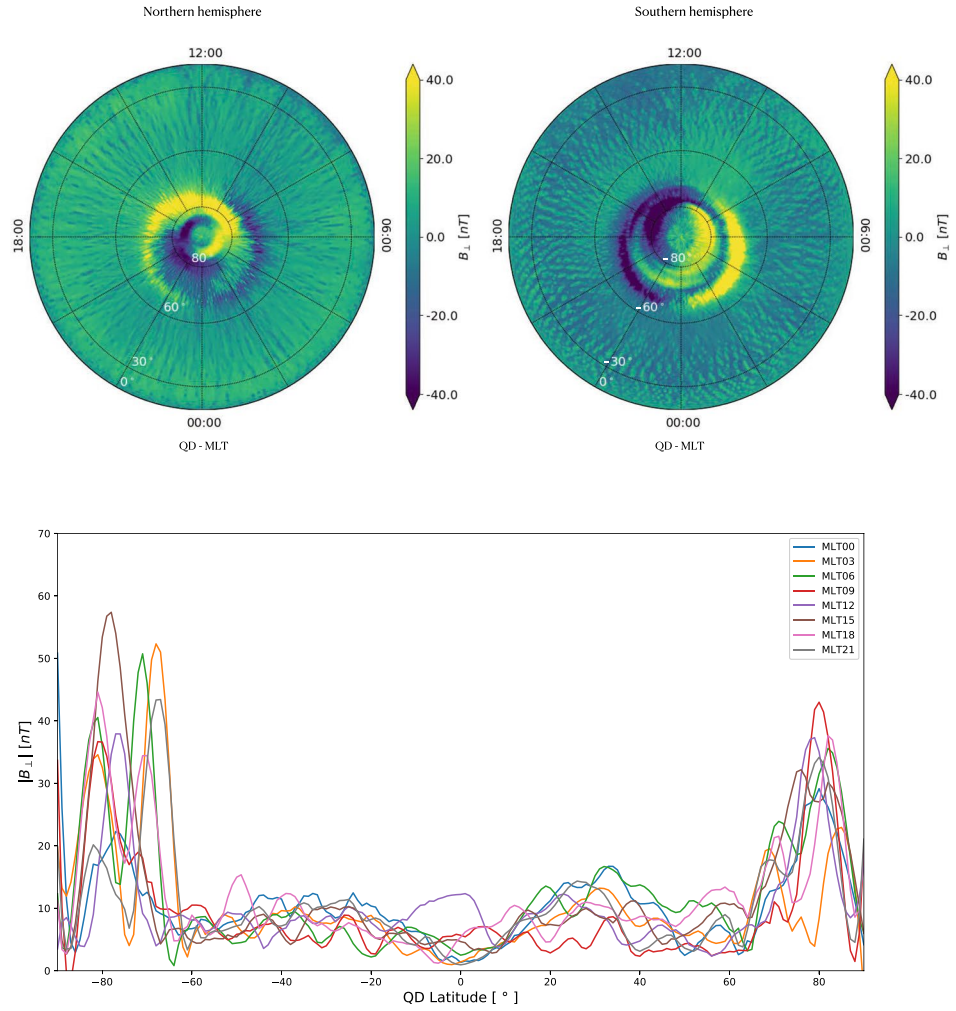
Figure 1. *Top:* climatological maps of signed geomagnetic field perpendicular to the direction of the main field, $\mathbf{B}_\perp$, in both hemispheres saturated between -40 and 40 nT. The sign of $\mathbf{B}_\perp$ is given by the sign of the West-East component; *Bottom:* $\mathbf{B}_\perp$ as a function of the quasi-dipole (QD) latitude at fixed magnetic local time (MLT) (different colors correspond to different MLTs). Curves are smoothed with a Savitzky-Golay filter (see the text).

2.2. The Electrical Conductivity

Electric currents in the ionosphere can be generated by neutral winds and electric fields, which drive electrons and ions in opposite directions. By assuming that, at Swarm heights, the ionospheric ions mostly consist of only one species (O^+) and their density is similar to that of electrons, namely $n_i \simeq n_e$, the electrical conductivity parallel $(\sigma_\parallel)$ and perpendicular (σ_P, σ_H) to the geomagnetic field can be written as

$$\sigma_\parallel = n_e e^2 \left(\frac{1}{m_e \nu_e} + \frac{1}{m_i \nu_i} \right) \tag{1}$$

$$\sigma_P = n_e e^2 \left[\frac{\nu_e}{m_e(\nu_e^2 + \Omega_e^2)} + \frac{\nu_i}{m_i(\nu_i^2 + \Omega_i^2)} \right] \tag{2}$$

$$\sigma_H = n_e e^2 \left[\frac{\Omega_e}{m_e(\nu_e^2 + \Omega_e^2)} + \frac{\Omega_i}{m_i(\nu_i^2 + \Omega_i^2)} \right], \tag{3}$$

where e is the electron charge, m_e, and m_i are the electron and ion mass, respectively, $\nu_e = \nu_{en} + \nu_{ei}$ and $\nu_i = \nu_{in} + \nu_{ie}$ are the collision frequencies of electrons and ions, respectively; the subscript marking the two species colliding (electrons, neutrals, and ions). The electron and ion gyrofrequencies are given by

$$\Omega_e = \frac{eB}{m_e} \qquad \Omega_i = \frac{eB}{m_i},$$

(4)

being B the magnetic field strength. As we can see, the definition of ionospheric conductivities implies a linear dependence on the electron density. However, due to the dependence of the electron-ion collision rates on both n_e and T_e, conductivities show a more complicated dependence (Kelley, 2009). In the high ionosphere, above ~ 180 km, the main mechanisms affecting the electron density in the dayside are the solar extreme ultraviolet (EUV) and the electron precipitation, together with other transport mechanisms coupling the magnetosphere and the ionosphere (Moen & Brekke, 1993; Wang et al., 2005). Above ~ 180 km Pedersen and Hall conductivities become rapidly unimportant (Moen & Brekke, 1990, 1993). For this reason, we will focus on the parallel component only.

In Equation 1, the first term in parenthesis is dominant, being $m_e \ll m_i$ and $\sigma_\parallel$ is directly proportional to the electron density and inversely proportional to the electron collision frequency (Cravens, 1997; Rishbeth, 1997). Aggarwal et al. (1979) modeled the electron collision frequency in the range of altitudes 50–500 km by using both experimental and theoretical values. They found that electron-ion collisions dominate above ~170 km, with the values changing with the solar activity and season. At ~100 km of altitude the effect of electron-neutral collision in the dayside is already negligible in computing conductivity (Vickrey et al., 1981). In the nightside the altitude at which the equality of electron-neutral and electron-ion collisions is reached is ~280 km at middle and high latitudes. At lower latitudes this altitude is higher. This implies that at Swarm altitudes and low nightside latitudes, although the electron-neutral collision frequency is still negligible, the uncertainty in considering only the electron-ion collisions is slightly larger. However, we will focus on the middle and high latitudes, where in the ionospheric F-layer the collision frequency is actually dominated by the electron-ion collision term, being $\nu_{ei} \gg \nu_{en}$ and $\nu_{ei} \gg \nu_{in}$ (Aggarwal et al., 1979; Kelley, 2009; Nicolet, 1953; Nishino et al., 1998; Singh, 1966; Takeda & Araki, 1985; Vickrey et al., 1981). As O^+ ions dominate in that ionospheric region, for the electron-ion collision frequency we can use the following relation (Kelley, 2009):

$$\nu_{ei} = n_e T_e^{-3/2} \left[34 + 4.18 ln \left(\frac{T_e^3}{n_e} \right) \right],$$

(5)

where n_e and T_e are the electron density and temperature, respectively. From Equation 5 it follows that the parallel electrical conductivity is

$$\sigma_\parallel = \frac{e^2 T_e^{3/2}}{\left[34 + 4.18 ln \left(\frac{T_e^3}{n_e} \right) \right] m_e}.$$

(6)

As we can see, electrical conductivity is particularly sensitive to electron temperature variations, due to the $\propto T_e^{3/2}$ dependence, and we expect to find common features in both physical quantities (Lomidze et al., 2018). This puts in relation the conductivity with the energy input (and eventually dissipation) of the ionospheric F-layer (Singh, 1966). As the parallel conductivity depends only on n_e and T_e, and these quantities can be directly measured by the Swarm mission, it is straightforward to obtain the parallel conductivity at Swarm altitudes by using Equation 6. In cgs units this quantity has the dimensions of $[s^{-1}]$. In what follows, when referring to the electrical conductivity we will implicitly consider only the direction parallel to the geomagnetic field.

3. Results and Discussion
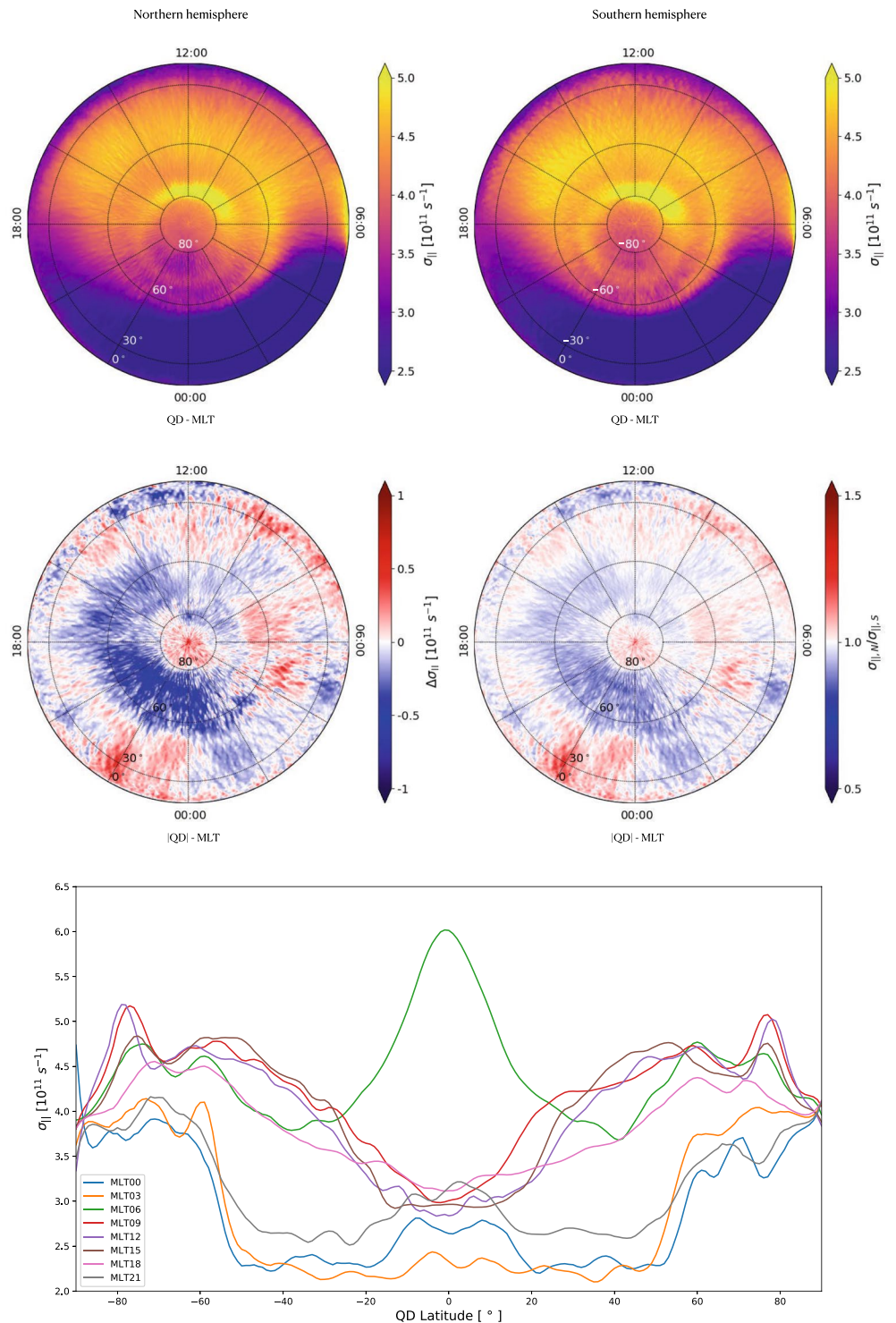
3.1. Climatological Maps of Electrical Conductivity

Maps of electrical conductivity have been realized with $1° \times 1°$ binning in QD latitude-MLT coordinates ($1°$ longitude corresponds to 4 min in MLT). Time series collected within each bin have been filtered out by using a median filter in order to remove spikes. The value representative of each bin corresponds to the median of the filtered series. Errors on electrical conductivity within each bin were computed by applying a bootstrap method. More in detail, the median value of conductivity was computed for 1,000 different subsets randomly extracted and sized at 60% of the total number of measurements falling into the bin. The error was assumed to be represented by the standard error on the median conductivities computed.

Climatological maps of electrical conductivity have been obtained by considering the whole 4-year data set at 1 Hz. The results are shown in Figure 2. Here, the electrical conductivity for both Northern (left) and Southern (right) Hemispheres saturated between 2.5 and 5.0×10^{11} s^{-1} is reported in the first row. The conductivity ranges between ~2.1 and $\sim 6 \times 10^{11}$ s^{-1}, has a maximum error (computed as explained above) of $\sim 0.6\%$, and is characterized by the existence of two maxima: at very high latitudes (around ±80°) between 09:00 and 12:00 MLT, in correspondence with the Region R0 and the polar magnetic cusp (Milan et al., 2017), and at low latitudes (within ±20°) around 06:00 MLT. The latter peak, which represents the absolute maximum value of $\sigma_\parallel$, corresponds to the morning overshoot (Stolle et al., 2011). This feature is associated with a sudden increase of T_e in passing from night to day at the dip equator due to the decrease of heat conduction, and reaches the minimum where the geomagnetic field is horizontal. Because of the strong dependence of electrical conductivity on T_e this feature is rather expected in our maps. The most general and evident feature emerging from these maps is the day-night conductivity asymmetry due to solar illumination. The effects of solar illumination and EUV ionization are indeed immediately recognizable in both hemispheres from 06:00 to 18:00 MLT (dayside) and between 30° and 60° QD latitude in both hemispheres.

The solar contribution is well represented by the behavior of the height-integrated Pedersen and Hall conductivity computed by Chapman (1956), namely $\Sigma_P \propto 5\sqrt{cos\chi}$ and $\Sigma_H \propto 10\sqrt{cos\chi}$, being χ the zenith angle that takes into account the local position of the Sun, i.e., its apparent elevation. The electrical conductivity reaches $\sim 4.8 \times 10^{11}$ s^{-1} at 15:00 MLT and ±50° QD latitude in both hemispheres. At QD latitudes between ±60° and ±80° the features associated with R1 and R2 are clearly visible especially in the nightside, where particle precipitation is the dominant process injecting energy in auroral regions and the effect of EUV ionization is almost absent. Particularly interesting is the drop of electrical conductivity between R1 and R2, where the particle dynamics is mainly governed by the intensification of horizontal Hall and Pedersen currents, which are a direct consequence of the coupling between magnetotail regions and the ionosphere in the nightside. These currents dissipate energy via Joule heating and are consequently responsible for a temperature increase occurring at altitudes (90–110 km) well below Swarm. For this reason, a drop instead of an enhancement of conductivity is observed at those latitudes.

The other steep increase of $\sigma_\parallel$, as we have anticipated, can be observed in the dayside sector between 09:00 and 15:00 MLT at $\sim \pm80°$ QD latitude, with a peak between 09:00 and 12:00 MLT. This feature is probably associated to the cusp region (Milan et al., 2017), where intense electron precipitation occurs and energy is deposited due to the coupling between the dayside (open) magnetosphere and the ionosphere (Brinton et al., 1978; Foster, 1983; Prölss, 2006). However, the electrical conductivity here computed shows remarkable differences with respect to Hall and Pedersen conductivities. For example, the nightside horizontal conductivities are estimated to be 1/10–1/30 times the noon values and the effect of the daily variation is observed to persist a few hours after the sunset (Kane, 1971; Maeda, 1977; Tarpley, 1970). Such a huge day-night asymmetry is not observed in our study for parallel conductivity, where the dayside conductivity is observed to be up to 2–3 times that in the nightside.

In the second row of Figure 2 the hemispheric asymmetry of electrical conductivity is reported. It has been computed in two ways: (1) the difference $\Delta\sigma_\parallel$ between the conductivity computed in the Northern Hemisphere, $\sigma_{\parallel,N}$, and that computed in the Southern one, $\sigma_{\parallel,S}$, respectively (on the left); (2) the ratio of the two conductivities, namely $\sigma_{\parallel,N} / \sigma_{\parallel,S}$. By looking at these maps, we can notice that the electrical conductivity in the Northern Hemisphere is slightly higher than in the Southern one at low QD latitudes in the premidnight

Figure 2. *Top:* climatological maps of electrical conductivity, $\sigma_\parallel$, in both hemispheres saturated between 2.5 and 5.0×10^{11} s^{-1}; *Middle:* climatological maps of conductivity asymmetry computed as the difference between the conductivities in Northern and Southern Hemispheres ($\Delta\sigma_\parallel$, on the left), and as the ratio between the two (on the right) saturated between -1 and 1 and between 0.5 and 1.5, respectively; *Bottom:* $\sigma_\parallel$ as a function of the QD latitude at fixed MLT (different colors correspond to different MLTs). Curves are smoothed with a Savitzky-Golay filter (see the text).

sector and at middle latitudes in the predawn sector, and higher (up to ∼1.5 times) in the polar cap. On the other hand, the same quantity is appreciably smaller (∼0.7 times) between ±60° and ±80° latitude in the premidnight sector, and in correspondence of the magnetic cusp in the dayside. As we have analyzed 4 years of data acquired by Swarm A satellite we cannot preclude the possibility that these asymmetries can be partially due to seasonal effects (Cnossen & Förster, 2016).

The location of all the features described so far for both hemispheres can be easily recognized after plotting $\sigma_\parallel$ as a function of the QD latitude for fixed MLTs. Such a plot is shown in the bottom panel of Figure 2, where the different colors of the solid curves correspond to different MLTs. Curves have been smoothed by using a 4th-order Savitzky-Golay low-pass filter with a smoothing window's size of 17 points (Savitzky & Golay, 1964). As we can see, the maximum conductivity occurs at the dip equator at 06:00 MLT, and corresponds to the morning overshoot. In contrast, the minimum conductivity occurs in the premidnight sector (from 21:00 to 00:00 MLT) between ±15° QD latitude in both hemispheres. At the same QD latitude but in the morning sector, $\sigma_\parallel$ is enhanced and increases quite smoothly poleward toward the auroral regions. The presence of Region 2 (Iijima & Potemra, 1978) marks the beginning of the auroral regions. The estimate of the location of such a region can be also obtained by looking at the curves reported on the plot of Figure 2 (lower panel) as well as the curves reported in the bottom panel of Figure 1. Moving from middle to high magnetic latitudes a steep increase in the slope of the curves can be observed, mostly at 00:00 and 03:00 MLT, at around ±60° QD latitude. In the same way, prominent peaks marking Region 1 can be observed at around ±80° QD latitude, especially in the prenoon sector, where the signature of the magnetic cusp is clearly visible (Milan et al., 2017). With a reasonable approximation we can identify the region among Regions 1 and 2 as the auroral regions. Interestingly, in this region, the electrical conductivity in the Southern Hemisphere is higher than in the Northern one, as evidenced both in the asymmetry maps of Figure 2 (middle panels) and in the height of the peaks reported on the plot of Figure 2 (lower panel).

3.2. Seasonal Variation of Electrical Conductivity

We investigated the seasonal variation of electrical conductivity in order to study its dependence on solar illumination. We portioned the entire data set according to the local season (i.e., the season at the position of the satellite) such that each year is divided into four periods 3-month long centered around equinoxes and solstices. In this way, the seasonal variation of electrical conductivity reflects the actual solar illumination conditions. Corresponding maps are reported in Figure 3, where four different panels, one for each local season, display the electrical conductivity for both hemispheres together with the asymmetries $\Delta\sigma_\parallel$ (on the left) and $\sigma_{\parallel,N} / \sigma_{\parallel,S}$ (on the right). Errors on conductivities were computed with the bootstrap method (see §3.1), which provided the following maximum values: ∼ 2.6% for spring, ∼ 3.1% for summer, ∼ 2.4% for autumn, and ∼ 3.0% for winter. As a general consideration, the electrical conductivity shows remarkable variations with the local season. Also, the hemispheric asymmetries are much more evident than in the climatological case. From spring (panel a) to summer (panel b), there is an increase of electrical conductivity in the dayside ionosphere at all MLTs, especially between the noon and the dusk at middle QD latitudes. An enhancement of conductivity is visible even in the nightside in the premidnight sector and at low latitudes. During the local autumn (panel c) and winter (panel d) the electrical conductivity marking the equatorward edge of the auroral regions is comparable or even higher than conductivity in the dayside, especially in the predawn and postdusk sectors and in the Southern Hemisphere. The separation between Regions 1 and 2 is clearly visible, especially in the winter and for both hemispheres. The winter nightside appears to be darker than in spring and summer, and at very high latitudes, in the polar cap, there is a dark feature slightly larger in the Northern Hemisphere than in the Southern one. It could be associated with the polar hole (Brinton et al., 1978), a region of decayed electron density due to the combined effect of lack of photoionization and a slow convection pattern. These findings are consistent with previous literature. Moen and Brekke (1993) modeled Pedersen and Hall conductivities in sunlit conditions to point out the dependence of photoelectrons' production by EUV on solar activity and zenith angle. This variation is reflected in the parallel conductivity. In fact, due to both the augmented production of photoelectrons and the electron precipitation associated with current systems flowing in the ionosphere and from (toward) the magnetosphere, also the density of FACs in the Region R1 was found to depend on solar illumination via the zenith angle and the
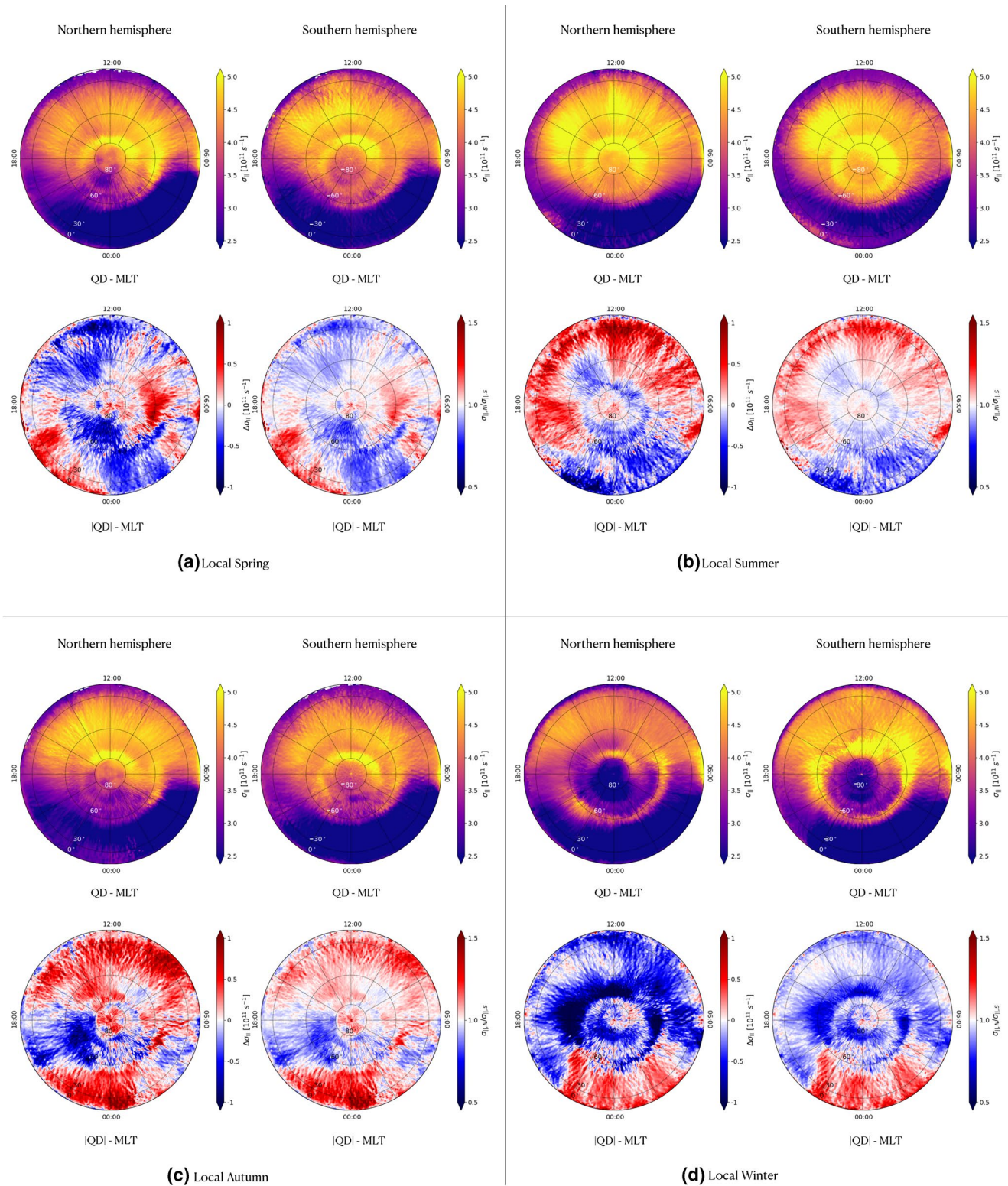
Figure 3. Seasonal maps of electrical conductivity. Clockwise from top left: (a) local spring, (b) summer, (c) autumn, and (d) winter. In each of the four panels we show $\sigma_{\parallel}$ in both hemispheres saturated between 2.5 and 5.0×10^{11} s^{-1} (top row), and the seasonal conductivity asymmetry computed as the difference between the conductivities in Northern and Southern Hemispheres ($\Delta\sigma_{\parallel}$, on the left), and as the ratio between the two (on the right) saturated between -1 and 1 and between 0.5 and 1.5, respectively (bottom row).

seasonal variations (Cattell et al., 2003; Fujii & Iijima, 1987; Fujii et al., 1981). For example, around noon FAC density in summer is twice than that in winter during quiet conditions (Christiansen et al., 2002; Fujii et al., 1981; Wang et al., 2005), and the auroral oval is shifted poleward of about $\sim 1-3°$. This feature is observed also in our data set in both hemispheres, with the only difference that it is not localized around noon but encloses all the MLTs in the dayside. In contrast, the dayside winter conductivity peaks in a restricted thinner region centered in the prenoon sector (around 11:00 MLT).

The hemispheric asymmetry also strongly varies with local seasons. In spring, electrical conductivity in the Southern Hemisphere is slightly higher than in the Northern one in the auroral regions mostly in the nightside, while it is appreciably lower in the dawn sector; during the summer electrical conductivity in the Southern Hemisphere is higher than in the Northern one in the auroral regions at all MLTs and at all latitudes in the nightside, while the Northern Hemisphere dominates in the dayside at low latitudes. In autumn, the electrical conductivity in the Northern Hemisphere is higher than in the Southern one at all latitudes and MLTs except in the postdusk sector. Finally, during winter a positive $\Delta\sigma_\parallel$ is observed only from 21:00 to 03:00 MLT at QD latitudes lower than 60°.

These findings confirm previous observations according to which the density of FACs, especially in Region 1, depends on solar illumination via the zenith angle and the seasonal variations (Cattell et al., 2003; Fujii & Iijima, 1987; Fujii et al., 1981).

3.3. The Contribution of Particle Precipitation to Electrical Conductivity

It is well known that the main contributions to parallel electrical conductivity in the ionosphere at high latitudes, which is associated to the intensification of FACs, are the enhancement of photoelectrons by EUV solar radiation and particle precipitation due to the magnetosphere-ionosphere coupling (Cogger et al., 1977; Collin et al., 1998; Liou et al., 1997; Liou et al., 2001; Meng & Lundin, 1986; Moen & Brekke, 1993; Newell et al., 1996). In previous sections we showed for the first time climatological maps of parallel electrical conductivity at Swarm altitude, and its seasonal variation. Of course, Swarm observations incorporate the contribution from all mechanisms participating to the onset of ionospheric conductivity.

The climatological contribution to electrical conductivity due to sunlit can be estimated by taking advantage of the International Reference Ionosphere (IRI) model at Swarm altitude. The IRI (Bilitza et al., 2017) is the empirical climatological model of the ionosphere that is, recognized as the official ISO standard for the ionosphere (Bilitza, 2018). IRI provides hourly monthly median values of the electron density, electron and ion temperature, and ion composition in the ionospheric altitude range, on a global basis, for different levels of solar and magnetic activity. In this study, climatological values of electron density and temperature modeled by IRI were used to obtain modeled values of the parallel electrical conductivity. Specifically, IRI was run for the same time period covered by Swarm A data set and with the same sampling rate, as if IRI values were co-located with measurements from Swarm A Langmuir probes. In this way, a perfect spatial and temporal consistency between measured and modeled data is guaranteed. The NeQuick topside option (Coïsson et al., 2009; Nava et al., 2008) has been applied for the description of the topside electron density profile shape, which has been shown to perform the best at Swarm satellite altitudes (Pignalberi et al., 2016). Topside electron density values are anchored to the F-layer peak whose electron density ($NmF2$) and height ($hmF2$) have been modeled through URSI coefficients (Rush, 1989) and Shubin et al. (2013) option, respectively. Because the magnetic activity dependence is not considered in this work, the IRI STORM options have been deactivated. For what concerns the modeling of the electron temperature, the Truhlik et al. (2012) model has been applied, which now includes also the solar activity dependence to the previous electron temperature model (Truhlik et al., 2000, 2009). In this model, electron temperature values at five anchor points located at 350, 550, 850, 1,400, and 2,000 km of altitude are modeled through a spherical harmonic expansion in a system of associated Legendre polynomials (up to the 8th order) in terms of MLT and INVDIP latitude. Coefficients of the spherical harmonic expansion were calculated for summer and winter solstices, and for combined equinoxes, regardless of the hemisphere; then, interhemispheric differences were not considered. The solar activity dependence was included by the selection of three solar activity ranges and the description of corresponding variability as a function of PF10.7 solar index (Truhlik et al., 2012). The complete vertical electron temperature profile is obtained by a linear interpolation be-

tween the anchor points and by applying Epstein-step functions to the transition from regions with different gradients, thus producing a continuous analytical representation of the electron temperature profile. It is worth mentioning that the scarce availability of electron temperature measurements in the topside ionosphere strongly limits a more refined description other than IRI does. As a consequence, the IRI electron temperature model does not describe small-scale spatial and temporal structures which are indeed observed by Swarm. Moreover, it should be noted that, historically, IRI has difficulty in predicting the plasma behavior at high latitudes because it relies mainly on data sets concerning mid and low latitudes.

By computing electron density and temperature with the IRI model at any satellite location, we can compute the electrical conductivity by using Equation 6 and obtain a model based on IRI, $\sigma_{\parallel,IRI}$ that takes into account mainly the contribution due to solar illumination. The results for both hemispheres are shown in the top panel of Figure 4. Errors on climatological conductivity derived from the IRI model within each bin were computed by using the bootstrap method (see §3.1), which provided a maximum value of $\sim 0.5\%$. When considering the maximum errors for each season (like in §3.2), we found the values $\sim 0.8\%$ for spring and winter, and $\sim 0.9\%$ for summer and autumn. There are three main features to point out: (1) there is an obvious day-night asymmetry generated by the local position of the Sun in terms of solar zenith angle. No features are present in the nightside, while in the dayside we can recognize peaks of conductivity in correspondence with the morning overshoot, at noon and in the postnoon sector. No auroral features emerge, as they are mainly due to particle precipitation not modeled by IRI; (2) in the dayside and at any MLT the values of electrical conductivity are appreciably lower than those obtained from Swarm observations and shown in the top panel of Figure 2. This is expected as the IRI model does not consider the energy exchange and injection from magnetosphere-ionosphere coupling due to precipitating particles; (3) the hemispheric asymmetry (not shown) is negligible except for the case of polar caps, as in different seasons they are not illuminated in the same way.

We remark that the IRI model does not explicitly take into account the contribution of the particle precipitation at high latitudes for both electron density and temperature modeling; specifically, no driver or index describing the particle precipitation was considered in the developing of the IRI model. However, it has to be considered that IRI is a climatological model whose main purpose is a reliable representation of the diurnal, seasonal, spatial, solar, and magnetic activity trends of several ionospheric parameters at climatological spatial and temporal scales. Then, not all the physical phenomena associated with the plasma dynamics are considered in IRI. Among them, the effects due to the particle precipitation at high latitudes. Thus, in principle, by subtracting the conductivity obtained through the IRI model to that computed from Swarm data, we could obtain a reasonable estimate of the contribution to conductivity mainly from particle precipitation. This factor is directly linked to FACs, so we can produce maps capable of pointing out some features that are typical of FACs. In particular, by subtracting from the climatological maps, reported on the top of Figure 2, the IRI maps, reported on the top of Figure 4, we obtain the maps shown in the middle panel of Figure 4. Here, the electrical conductivity ranges between ~ 0.5 to $\sim 2.8 \times 10^{11}$ s^{-1}. The errors on the subtracted maps are of the order of the squared root of the sum of their variances. Thus, for the climatological maps in the middle panel of Figure 4 the maximum error is $\sim 0.8\%$. In both hemispheres, particle precipitation is the responsible for the conductivity features in the nightside, especially at auroral QD latitudes. In the Southern Hemisphere there is an enhancement through all night in the Region R2 and an enhancement in correspondence of the Region R1 in the prenoon hours. In the dayside, at latitudes of $\sim 80°$ in the morning sector, we recognize the features associated with the magnetic polar cusp (Milan et al., 2017), which are not recognizable in the maps obtained via the IRI model. Very interesting is also the presence of an enhanced equatorial feature at 06:00 MLT, that corresponds to the morning overshoot. This feature gives an indication about the role played by particle precipitation in the enhancement of electron temperature at the equatorial dawn. These findings confirm under both an observational (through Swarm observations) and modeling (through the IRI model) point of view the key role played by particle precipitation in producing the auroral features, supporting the strong connection between magnetosphere and ionosphere in the nightside (via the magnetotail-ionosphere coupling at all MLTs from dusk to dawn and QD latitudes higher than 60°) and in the dayside (via the injection of particles into the cusp).

The location of all the features described for both hemispheres can be, again, recognized in the plot on the bottom panel of Figure 4. Likewise Figure 2, curves are smoothed by a 4th-order Savitzky-Golay low-pass
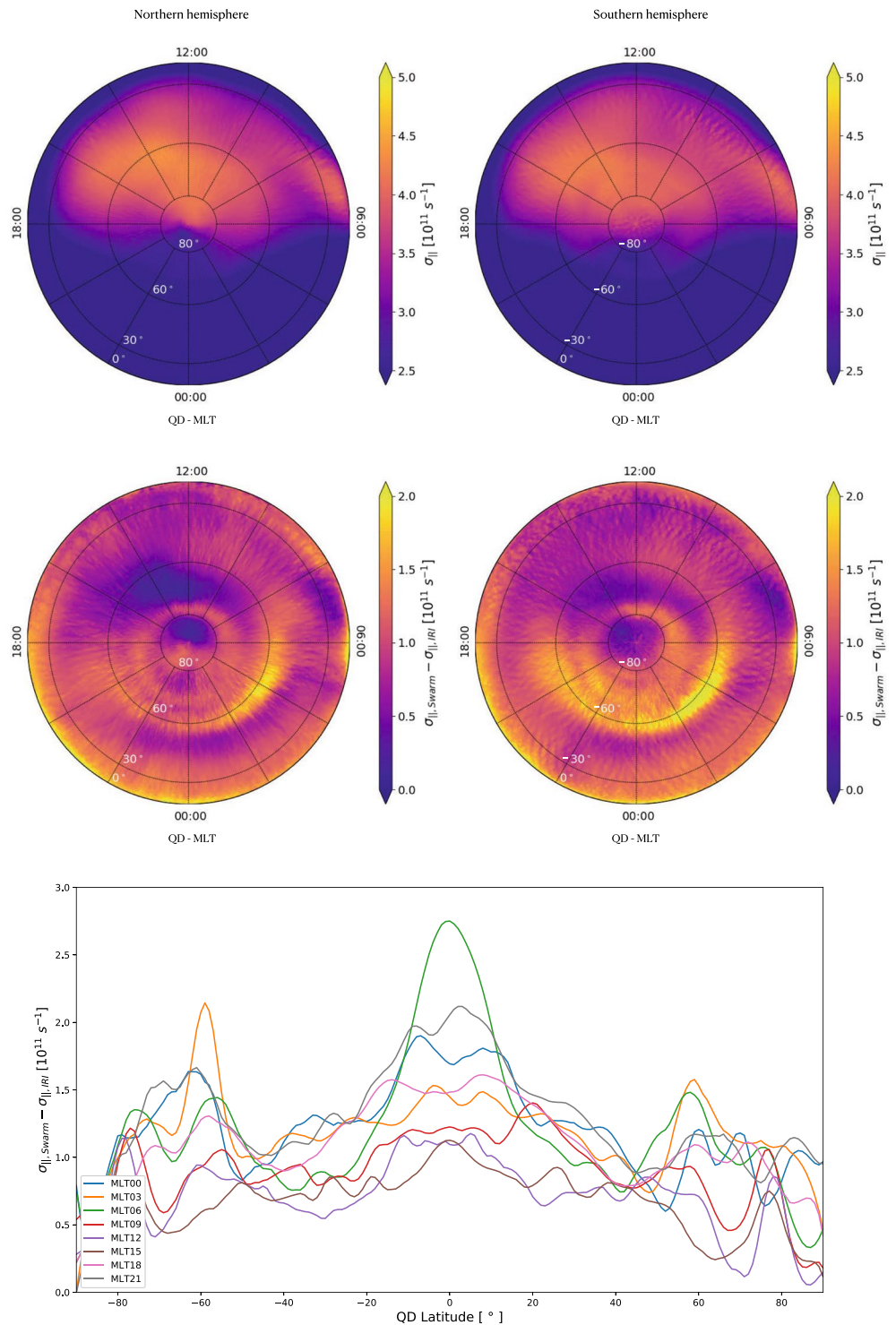
Figure 4. *Top:* International Reference Ionosphere (IRI) modeling of electrical conductivity, $\sigma_\parallel$, in both hemispheres saturated between 2.5 and 5.0×10^{11} s^{-1}; *Middle:* climatological maps of the contribution to conductivity mainly from particle precipitation computed as the difference between the conductivities retrieved using Swarm data and those from IRI model, namely $\sigma_{\parallel,Swarm} - \sigma_{\parallel,IRI}$ saturated between 0 and 2×10^{11} s^{-1}; *Bottom:* electrical conductivity mainly from particle precipitation as a function of QD latitude at fixed MLT (different colors correspond to different MLTs). Curves were smoothed with a Savitzky-Golay filter (see the text).

filter with a smoothing window's size of 17 points (Savitzky & Golay, 1964). Also in this case the maximum conductivity occurs at the dip equator at 06.00 MLT, and corresponds to the morning overshoot. In this case, the minimum conductivity occurs in the postnoon sector (from 12:00 to 15:00 MLT) between 60° and 80° QD latitude in both hemispheres. This region corresponds closely to the location of maximum $\sigma_{\parallel,IRI}$. A secondary very pronounced peak of conductivity occurs at 03:00 at 60° latitude, and according to the same criteria used in Figure 2, marks the equatorward part of Region R2. This region is characterized mainly by an intense particle precipitation occurring in coincidence of a FAC flowing toward the ionosphere (Iijima & Potemra, 1978). Other peaks marking Region R1 start at about ±80° QD latitude in the nightside, and increase slightly moving toward the dayside. This is consistent with the observation of Region R1 at little higher latitudes in the dayside than in the nightside. Also in this case of mainly particle precipitation, in auroral regions the enhancement of electrical conductivity in the Southern Hemisphere is higher than in the Northern one, and the electron precipitation is asymmetric, being the hemispheric asymmetry well represented in the middle panel of Figure 2.

In Figure 5 we show the seasonal behavior of electrical conductivity mainly due to particle precipitation in both hemispheres (Northern on the left, Southern on the right) saturated between 0 and 2×10^{11} s^{-1}. The maximum errors on the subtracted seasonal maps are of the order of ~ 2.7% for spring, ~ 3.2% for summer, ~ 2.6% for autumn, and ~ 3.1% for winter. Moving from summer to winter, the conductivity in the equatorward edge of the auroral regions (at about 60°) enhances in the nightside from dusk to 08:00 MLT, while is lower at the same latitude in the dayside. As it is known, the ionospheric conductivity is expected to change as a function of solar zenith angle (Moen & Brekke, 1993) and therefore the summer and winter polar regions can have dramatic different conductivity values. In our case, the conductivity changes by a factor of 2 around the pole, thus confirming the dependence of the FACs on seasonal changes (Papitashvili et al., 2002). It has been found, for example using Orsted satellite magnetic field measurements that, statistically, there is a factor of 1.6 between the summer and winter maximum FAC density (Papitashvili et al., 2002). Also Wang et al. (2005) showed that the maximum FAC changes by approximately a factor of 2 from summer to winter in the dayside. Thus, from previous studies, it can be concluded that FACs change from winter to summer by about a factor of 2 as we find in our maps (Christiansen et al., 2002; Fujii et al., 1981) and the auroral regions are located poleward of about ~ 1 − 3°. This suggests that while particle precipitation is more and more effective in the nightside in approaching the local winter, at the same time EUV photoionization becomes more and more important in the dayside. The only exception is represented by the cusp region around noon. In spring and summer the conductivity in this small region is comparable with that in the nightside, reaching a peak of about 2×10^{11} s^{-1} in the summer Southern Hemisphere, then it dims in autumn and winter, appearing less structured in the Southern Hemisphere. The only sector in the nightside where conductivity is appreciably high during all seasons in both hemispheres is that between 02:00 and 05:00 MLT, suggesting that in this region the ionospheric precipitation processes are almost always effective. This arch is present in summer and well visible mainly in the Southern Hemisphere. In spring and autumn it enlarges to midnight hours, and expands from dusk to 08:00 MLT, while in winter it reaches the maximum expansion and is characterized by an increased conductivity. In all seasons, excluding local exceptions, conductivity in the Southern Hemisphere is higher than in the Northern one. These findings confirm previous results and suggest that electron precipitation events are reduced in sunlight (Newell et al., 1996), except in the cusp, and show a suppression much more effective in the dayside winter than in summer (Liou et al., 1997, 2001). This is consistent with the fact that while the nightside auroras are suppressed in summer due to the decrease of energy of precipitating electrons, dayside ones are enhanced in summer due to the increase of the electron flux number (Liou et al., 2001). Consistently, Collin et al. (1998) observed upflowing ion beams (precursors of electron precipitation) between 15:00 and 01:00 MLT with an occurrence peak in the premidnight winter and a minimum in summer. Swarm observations and the subtraction of the IRI model allow us to refine this conclusion and argue that the region of precipitating electrons extends from dusk to 08:00 MLT, with prominent peaks in the predawn autumn in the Northern Hemisphere, in the premidnight and predawn autumn in the Southern Hemisphere, in the winter nightside in both the hemisphere, especially the Southern one.
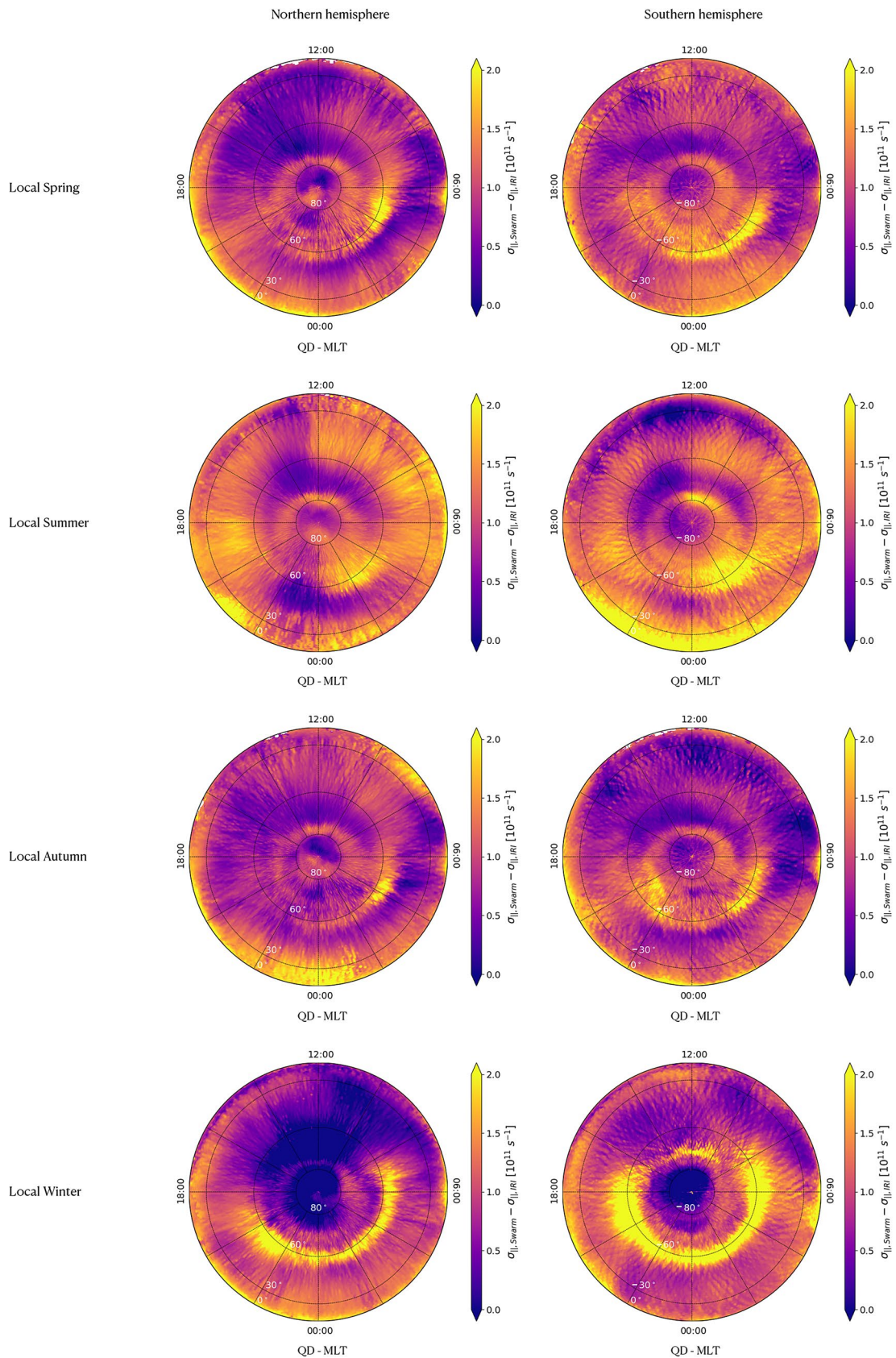
4. Summary and Conclusions

The main goal of the current study was to determine some properties of the electrical conductivity parallel to the geomagnetic field in the ionosphere at Swarm altitude. When considering climatological conductivity maps based on 4 years of observations we found that:

- Two conductivity maxima occur: one at very high QD latitudes (at ∼ 80°) around noon and one at low latitudes (within ±20°) at dawn; which may be associated to the R1 and the cusp region (Milan et al., 2017) and the morning overshoot (Stolle et al., 2011), respectively
- There is an evident and expected conductivity asymmetry from day to night. In the dayside the effect of solar EUV is dominant and conductivity has a peak at 15:00 MLT and at ±50° QD latitude. A peak between 09:00 and 12:00 MLT at around 80° is observed and may be associated with the cusp region; in the nightside particle precipitation is the dominant process injecting energy in the auroral regions and conductivity shows features between ±60° and ±80° that are associated with Regions R1 and R2
- There is an evident hemispheric asymmetry for which electrical conductivity in the Northern Hemisphere is higher than in the Southern one at low QD latitudes in the premidnight sector, at middle latitudes in the predawn sector, and in the polar cap. On the contrary, it is lower between ±60° and ±80° in the premidnight sector at the same QD latitudes as the dayside cusp

When considering the seasonal conductivity variation in order to study its dependence on solar illumination we found that:

- Electrical conductivity in the Southern Hemisphere is remarkably higher than that in the Northern one mainly during the summer nightside and the winter dayside
- Electrical conductivity increases from local spring to summer, especially in the dayside between noon and dusk at middle QD latitudes
- During local autumn and winter the electrical conductivity at auroral QD latitudes corresponding to Region 2 in the nightside is comparable or even higher than that in the dayside
- In correspondence of Regions R1 and R2 there is an enhancement of conductivity especially in the winter Southern Hemisphere
- The hemispheric asymmetry also depends on the local season in a complicated way

When focusing on the estimated contribution of particle precipitation to electrical conductivity, we found that:

- Conductivity features mainly from precipitations are greatly enhanced in the nightside, especially in the Southern Hemisphere, at QD latitudes in correspondence of the Regions R1 (in the prenoon hours) and R2 (the whole night), where intense particle flows are expected due to FACs
- Features characteristic of the polar cusp at high QD latitudes and the morning overshoot at low latitudes are recognizable in the dayside at around noon and at 06:00, respectively
- Moving from spring to winter the conductivity at ∼ 60° QD latitude increases, from dusk to 08:00 MLT (which corresponds to the region of precipitating electrons) changing by a factor of ∼2 around the pole, while in the dayside the conductivity lowers. This suggests that, when approaching to winter, particle precipitation is more effective in the nightside sector, while EUV photoionization is more important in the dayside, being the only exception the cusp region, which becomes dimmer and dimmer from spring to winter

These results are consistent with previous literature, according to which electron precipitation events are suppressed in sunlight except in the cusp, with a suppression more effective in winter than in summer. While auroras are suppressed in the summer nightside due to the decrease of energy of the precipitating particles, they are enhanced in the summer dayside due to the increasing number of particles precipitating. Moreover, the augmented production of photoelectrons and electrons precipitation associated with FACs depends on solar illumination via the zenith angle and the seasonal variations.

Figure 5. Seasonal maps of electrical conductivity when the main cause is particle precipitation in both hemispheres (Northern on the left, Southern on the right). From top to bottom: Local spring, summer, autumn, winter. Saturation is between 0 and 2×10^{11} s^{-1}.

The insights gained from this study may be of interest for different reasons. First, the estimated electron precipitation, which is associated with FACs and causes the generation of auroras in the high-latitude ionosphere, is a mechanism effective in increasing electrical conductivity and the possible following amplification of FACs. For this reason, characterizing electrical conductivity may help to study the interaction between the magnetized plasma of solar origin carried on by solar wind and/or coronal mass ejections and the geomagnetic field. Second, to our knowledge, a statistical study focused on parallel electrical conductivity is lacking, despite this physical quantity plays a fundamental role in the amplification, evolution and dissipation of FACs in the high-latitude ionosphere, and thus in the space weather framework. For the first time, a statistical study performed by taking advantage of in-situ measurements has allowed us to show the features of electrical conductivity in the topside ionosphere. The 4 years of Swarm electron density and temperature measurements between 2014 and 2018 at 1 Hz permitted us both a climatological and a seasonal study. Third, for the first time we estimated the contribution of particle precipitation to electrical conductivity. To accomplish this task we subtracted the contribution of EUV photoionization modeled by the IRI model to what we obtained on the basis of Swarm observations. We stress that the results presented in this work are fully consistent with previous works in the literature (Christiansen et al., 2002; Fujii et al., 1981; Moen & Brekke, 1993; Newell et al., 1996; Papitashvili et al., 2002; Wang et al., 2005, just to mention a few). This strengthens the hypothesis that subtracting IRI model to Swarm observations in order to investigate the features of conductivity attributed to particle precipitation is robust and reasonable.

Regarding the future perspectives, there are several points that it would be interesting to deepen. Estimations of FACs via Ampere law were used to recover the position of the oval, which strongly depends on the geomagnetic activity level. Wang et al. (2005) found that during quiet conditions in the Southern Hemisphere the auroral oval can be fitted by an ellipse centered at −86.6° MLAT and 23.8 MLT, with size of semimajor axis 18.3°, semiminor axis 16.7° and the semimajor axis rotated clockwise by 2.9°. During quiet conditions upward FACs are observed between 13:00 and 14:00 MLT and downward ones between 09:00 and 11:00 MLT. During disturbed periods FACs move away from noon by about 2 h accordingly to the position of Region 1 identified by Iijima and Potemra (1978). In addition, the intensity of FACs is also modulated by the solar cycle, as measured by the F10.7 proxy (Ohtani et al., 2014). These few examples point out the necessity of investigating the variation of electrical conductivity associated with FACs as a function of the geomagnetic activity. For this reasons, the variation of electrical conductivity with both the geomagnetic activity level and the solar cycle will be investigated in a future work.

Another interesting question to be answered is the link between electrical conductivity features and ionospheric irregularities. Although the largest contribution to conductivity comes from electron temperature, the dependence on electron density remains, and the observed conductivity variations and gradients may be linked to the occurrence of ionospheric irregularities. Among the main sources of irregularities in the ionospheric F-layer at high latitudes we mention (Keskinen & Ossakow, 1983):

- Particle precipitation. Low-energy ($10^2 - 10^3$ eV) electrons are known to deposit most of their energy in the F-layer at high latitudes (Rees, 1963), especially in the polar cusp and in the prenoon sector at lower latitudes (Dyson & Winningham, 1974). Large scale convecting plasma enhancements have been observed in the midnight sector of the auroral F region due to particle precipitation and associated FACs (Vickrey et al., 1980)
- Plasma macro-instabilities. Sources of free energy giving rise to irregularities have been found in density gradients, velocity shears, and currents
- Waves. Quasi-periodic fluctuations in n_e and T_e were observed due to, for example, gravity waves (Hines, 1960). These waves can be in principle driven by Joule heating and Lorentz forces associated with electrojets and intense particle precipitations

The link between conductivity and ionospheric irregularities will be studied in a following work to shed light on their role in the onset and evolution of FAC signatures.

Another possible future study may be focused on the theoretical modeling of the contribution to conductivity due to particle precipitation, for example, by using a physical model such as a GCM model (http://www.hao.ucar.edu/modeling/tgcm/), and its comparison with the results obtained by current in situ obser-

vations. This would also allow separating the contribution of precipitations from other, if any, effects and eventually quantify their weight in the estimation of conductivity.

Finally, the scaling properties of electrical conductivity should be studied to understand the mechanisms participating in its variation and how this is effective in the dissipation of the energy incoming from the solar plasma and the magnetosphere. All these aspects will be approached in future works.

Data Availability Statement

The results presented rely on data collected by one of the three satellites of the Swarm constellation. We thank the European Space Agency (ESA) that supports the Swarm mission. Swarm data can be accessed at http://earth.esa.int/swarm.

References

Aggarwal, K., Nath, N., & Setty, C. (1979). Collision frequency and transport properties of electrons in the ionosphere. *Planetary and Space Science*, *27*(6), 753–768. https://doi.org/10.1016/0032-0633(79)90004-7

Amm, O. (1997). Ionospheric elementary current systems in spherical coordinates and their application. *Journal of Geomagnetism and Geoelectricity*, *49*(7), 947–955. https://doi.org/10.5636/jgg.49.947

Amm, O., Vanhamki, H., Kauristie, K., Stolle, C., Christiansen, F., Haagmans, R., et al. (2015). A method to derive maps of ionospheric conductances, currents, and convection from the Swarm multisatellite mission. *Journal of Geophysical Research: Space Physics*, *120*(4), 3263–3282. https://doi.org/10.1002/2014JA020154

Bilitza, D. (2018). IRI the International Standard for the Ionosphere. *Advances in Radio Science*, *16*, 1–11. https://doi.org/10.5194/ars-16-1-2018

Bilitza, D., Altadill, D., Truhlik, V., Shubin, V., Galkin, I., Reinisch, B., & Huang, X. (2017). International Reference Ionosphere 2016: From ionospheric climate to real-time weather predictions. *Space Weather*, *15*(2), 418–429. https://doi.org/10.1002/2016SW001593

Boström, R. (1964). A model of the auroral electrojects. *Journal of Geophysical Research*, *69*(23), 4983–4999. https://doi.org/10.1029/JZ069i023p04983

Boteler, D. H., & Pirjola, R. J. (2017). Modeling geomagnetically induced currents. *Space Weather*, *15*(1), 258–276. https://doi.org/10.1002/2016SW001499

Boteler, D. H., Pirjola, R. J., & Nevanlinna, H. (1998). The effects of geomagnetic disturbances on electrical systems at the Earth's surface. *Advances in Space Research*, *22*(1), 17–27. https://doi.org/10.1016/S0273-1177(97)01096-X

Brekke, A., & Hall, C. (1988). Auroral ionospheric quiet summer time conductances. *Annales Geophysicae*, *6*(4), 361–375.

Brinton, H. C., Grebowsky, J. M., & Brace, L. H. (1978). The high-latitude winter F region at 300 km: Thermal plasma observations from AE-C. *Journal of Geophysical Research*, *83*(A10), 4767–4776. https://doi.org/10.1029/JA083iA10p04767

Cattell, C., Dombeck, J., Peria, W., Strangeway, R., Elphic, R., & Carlson, C. (2003). Fast Auroral Snapshot observations of the dependence of dayside auroral field-aligned currents on solar wind parameters and solar illumination. *Journal of Geophysical Research*, *108*(A3), 1112. https://doi.org/10.1029/2001JA000321

Chapman, S. (1956). The electrical conductivity of the ionosphere: A review. *Il Nuovo Cimento*, *4*(S4), 1385–1412. https://doi.org/10.1007/BF02746310

Christiansen, F., Papitashvili, V. O., & Neubert, T. (2002). Seasonal variations of high-latitude field-aligned currents inferred from Ørsted and Magsat observations. *Journal of Geophysical Research*, *107*(A2), SMP 5-1–SMP 5-13. https://doi.org/10.1029/2001JA900104

Cnossen, I., & Förster, M. (2016). North-south asymmetries in the polar thermosphere-ionosphere system: Solar cycle and seasonal influences. *Journal of Geophysical Research: Space Physics*, *121*(1), 612–627. https://doi.org/10.1002/2015JA021750

Cogger, L. L., Murphree, J. S., Ismail, S., & Anger, C. D. (1977). Characteristics of dayside 5577Å and 3914Å aurora. *Geophysical Research Letters*, *4*(10), 413–416. https://doi.org/10.1029/GL004i010p00413

Coïsson, P., Nava, B., & Radicella, S. M. (2009). On the use of NeQuick topside option in IRI-2007. *Advances in Space Research*, *43*(11), 1688–1693. https://doi.org/10.1016/j.asr.2008.10.035

Collin, H. L., Peterson, W. K., Lennartsson, O. W., & Drake, J. F. (1998). The seasonal variation of auroral ion beams. *Geophysical Research Letters*, *25*(21), 4071–4074. https://doi.org/10.1029/1998GL900090

Cowley, S., Davies, J., Grocott, A., Khan, H., Lester, M., McWilliams, K., et al. (2003). Solar–wind–magnetosphere–ionosphere interactions in the Earth's plasma environment. *Philosophical Transactions of the Royal Society A Mathematical, Physical and Engineering Sciences*, *361*(1802), 113. https://doi.org/10.1098/rsta.2002.1112

Cravens, T. E. (1997). *Physics of solar system plasmas*. Cambridge: Thomas E. Cravens.

de la Beaujardiere, O., Alcayde, D., Fontanari, J., & Leger, C. (1991). Seasonal dependence of high-latitude electric fields. *Journal of Geophysical Research*, *96*(A4), 5723–5735. https://doi.org/10.1029/90JA01987

Dyson, P. L., & Winningham, J. D. (1974). Top side ionospheric spread F and particle precipitation in the day side magnetospheric clefts. *Journal of Geophysical Research*, *79*(34), 5219–5230. https://doi.org/10.1029/JA079i034p05219

Emmert, J. T., Richmond, A. D., & Drob, D. P. (2010). A computationally compact representation of Magnetic-Apex and Quasi-Dipole coordinates with smooth base vectors. *Journal of Geophysical Research*, *115*(A8), 322. https://doi.org/10.1029/2010JA015326

Finlay, C. C., Olsen, N., Kotsiaros, S., Gillet, N., & Tøffner-Clausen, L. (2016). Recent geomagnetic secular variation from Swarm and ground observatories as estimated in the CHAOS-6 geomagnetic field model. *Earth, Planets and Space*, *68*(1), 112. https://doi.org/10.1186/s40623-016-0486-1

Föpl, H., Haerendel, G., Haser, L., Lst, R., Melzner, F., Meyer, B., et al. (1968). Preliminary results of electric field measurements in the auroral zone. *Journal of Geophysical Research*, *73*(1), 21–26. https://doi.org/10.1029/JA073i001p00021

Foster, J. C. (1983). An empirical electric field model derived from Chatanika radar data. *Journal of Geophysical Research*, *88*(A2), 981–987. https://doi.org/10.1029/JA088iA02p00981

Friis-Christensen, E., Lhr, H., & Hulot, G. (2006). Swarm: A constellation to study the Earth's magnetic field. *Earth, Planets and Space*, *58*(4), 351–358. https://doi.org/10.1186/BF03351933

Fujii, R., & Iijima, T. (1987). Control of the ionospheric conductivities on large-scale Birkeland current intensities under geomagnetic quiet conditions. *Journal of Geophysical Research*, *92*(A5), 4505–4513. https://doi.org/10.1029/JA092iA05p04505

Fujii, R., Iijima, T., Potemra, T. A., & Sugiura, M. (1981). Seasonal dependence of large-scale Birkeland currents. *Geophysical Research Letters*, *8*(10), 1103–1106. https://doi.org/10.1029/GL008i010p01103

Fuller-Rowell, T. J., & Evans, D. S. (1987). Height-integrated Pedersen and Hall conductivity patterns inferred from the TIROS-NOAA satellite data. *Journal of Geophysical Research*, *92*(A7), 7606–7618. https://doi.org/10.1029/JA092iA07p07606

Germany, G. A., Torr, D. G., Richards, P. G., Torr, M. R., & John, S. (1994). Determination of ionospheric conductivities from FUV auroral emissions. *Journal of Geophysical Research*, *99*(A12), 23297–23305. https://doi.org/10.1029/94JA02038

Harang, L. (1946). The mean field of disturbance of polar geomagnetic storms. *Terrestrial Magnetism and Atmospheric Electricity*, *51*(3), 353. https://doi.org/10.1029/TE051i003p00353

Hines, C. O. (1960). Internal atmospheric gravity waves at ionospheric heights. *Canadian Journal of Physics*, *38*(11), 1441–1481. https://doi.org/10.1139/p60-150

Holzworth, R. H., Kelley, M. C., Siefring, C. L., Hale, L. C., & Mitchell, J. D. (1985). Electrical measurements in the atmosphere and the ionosphere over an active thunderstorm: 2. Direct current electric fields and conductivity. *Journal of Geophysical Research*, *90*(A10), 9824–9830. https://doi.org/10.1029/JA090iA10p09824

Hones, E. W. (1979). Solar wind-magnetosphere-ionosphere coupling. In B. M. McCormac & T. A. Seliga (Eds.), *Solar-terrestrial influences on weather and climate* (pp. 83–100). Dordrecht: Springer Netherlands.

Horton, W., Smith, J., Weigel, R., Crabtree, C., Doxas, I., Goode, B., & Cary, J. (1999). The solar-wind driven magnetosphere-ionosphere as a complex dynamical system. *Physics of Plasmas*, *6*(11), 4178–4184. https://doi.org/10.1063/1.873683

Iijima, T., & Potemra, T. A. (1978). Large-scale characteristics of field-aligned currents associated with substorms. *Journal of Geophysical Research*, *83*(A2), 599–615. https://doi.org/10.1029/JA083iA02p00599

Kamide, Y., & Baumjohann, W. (1993). *Magnetosphere-ionosphere coupling* (Vol. 23). Berlin, Heidelberg: Springer-Verlag Berlin Heidelberg. https://doi.org/10.1007/978-3-642-50062-6

Kamide, Y., Richmond, A. D., & Matsushita, S. (1981). Estimation of ionospheric electric fields, ionospheric currents, and field-aligned currents from ground magnetic records. *Journal of Geophysical Research*, *86*(A2), 801–813. https://doi.org/10.1029/JA086iA02p00801

Kane, R. (1971). Relationship between H ranges at equatorial and middle latitudes. *Journal of Atmospheric and Terrestrial Physics*, *33*(3), 319–327. https://doi.org/10.1016/0021-9169(71)90137-1

Kelley, M. (2009). *The Earth's ionosphere: Plasma physics and electrodynamics*, San Diego: Elsevier Science. Retrieved from https://books.google.it/books?id=3GlWQnjBQNgC

Keskinen, M. J., & Ossakow, S. L. (1983). Theories of high-latitude ionospheric irregularities: A review. *Radio Science*, *18*(6), 1077–1091. https://doi.org/10.1029/RS018i006p01077

Kirkwood, S., Opgenoorth, H., & Murphree, J. (1988). Ionospheric conductivities, electric fields and currents associated with auroral substorms measured by the EISCAT radar. *Planetary and Space Science*, *36*(12), 1359–1380. https://doi.org/10.1016/0032-0633(88)90005-0

Knudsen, D. J., Burchill, J. K., Buchert, S. C., Eriksson, A. I., Gill, R., Wahlund, J.-E., et al. (2017). Thermal ion imagers and Langmuir probes in the Swarm electric field instruments. *Journal of Geophysical Research: Space Physics*, *122*(2), 2655–2673. https://doi.org/10.1002/2016JA022571

Laundal, K. M., & Richmond, A. D. (2017). Magnetic coordinate systems. *Space Science Reviews*, *206*(1), 27–59. https://doi.org/10.1007/s11214-016-0275-y

Liou, K., Newell, P. T., & Meng, C.-I. (2001). Seasonal effects on auroral particle acceleration and precipitation. *Journal of Geophysical Research*, *106*(A4), 5531–5542. https://doi.org/10.1029/1999JA000391

Liou, K., Newell, P. T., Meng, C.-I., Brittnacher, M., & Parks, G. (1997). Synoptic auroral distribution: A survey using Polar ultraviolet imagery. *Journal of Geophysical Research*, *102*(A12), 27197–27205. https://doi.org/10.1029/97JA02638

Liu, H., & Lühr, H. (2005). Strong disturbance of the upper thermospheric density due to magnetic storms: CHAMP observations. *Journal of Geophysical Research*, *110*, S29. https://doi.org/10.1029/2004JA010908

Lomidze, L., Knudsen, D. J., Burchill, J., Kouznetsov, A., & Buchert, S. C. (2018). Calibration and validation of Swarm plasma densities and electron temperatures using groundbased radars and satellite radio occultation measurements. *Radio Science*, *53*(1), 15–36. https://doi.org/10.1002/2017RS006415

Lyon, J. G. (2000). The solar wind-magnetosphere-ionosphere system. *Science*, *288*(5473), 1987–1991. https://doi.org/10.1126/science.288.5473.1987

Maeda (1977). Conductivity and drifts in the ionosphere. *Journal of Atmospheric and Terrestrial Physics*, *39*(9), 1041–1053. https://doi.org/10.1016/0021-9169(77)90013-7

Marklund, G., Sandahl, I., & Opgenoorth, H. (1982). A study of the dynamics of a discrete auroral arc. *Planetary and Space Science*, *30*(2), 179–197. https://doi.org/10.1016/0032-0633(82)90088-5

Mende, S. B., Eather, R. H., Rees, M. H., Vondrak, R. R., & Robinson, R. M. (1984). Optical mapping of ionospheric conductance. *Journal of Geophysical Research*, *89*(A3), 1755–1763. https://doi.org/10.1029/JA089iA03p01755

Meng, C.-I., & Lundin, R. (1986). Auroral morphology of the midday oval. *Journal of Geophysical Research*, *91*(A2), 1572–1584. https://doi.org/10.1029/JA091iA02p01572

Milan, S., Clausen, L., Coxon, J., Carter, J., Walach, M.-T., Laundal, K. M., et al. (2017). Overview of solar wind–magnetosphere–ionosphere–atmosphere coupling and the generation of magnetospheric currents. *Space Science Reviews*, *206*, 547–573. https://doi.org/10.1007/s11214-017-0333-0

Moen, J., & Brekke, A. (1990). On the importance of ion composition to conductivities in the auroral ionosphere. *Journal of Geophysical Research*, *95*(A7), 10687–10693. https://doi.org/10.1029/JA095iA07p10687

Moen, J., & Brekke, A. (1993). The solar flux influence on quiet time conductances in the auroral ionosphere. *Geophysical Research Letters*, *20*(10), 971–974. https://doi.org/10.1029/92GL02109

Mozer, F. S., & Serlin, R. (1969). Magnetospheric electric field measurements with balloons. *Journal of Geophysical Research*, *74*(19), 4739–4754. https://doi.org/10.1029/JA074i019p04739

Nava, B., Cosson, P., & Radicella, S. (2008). A new version of the NeQuick ionosphere electron density model. *Journal of Atmospheric and Solar-Terrestrial Physics*, *70*(15), 1856–1862. https://doi.org/10.1016/j.jastp.2008.01.015

Newell, P. T., Meng, C.-I., & Lyons, K. M. (1996). Suppression of discrete aurorae by sunlight. *Nature*, *381*(6585), 766–767. https://doi.org/10.1038/381766a0

Nicolet, M. (1953). The collision frequency of electrons in the ionosphere. *Journal of Atmospheric and Terrestrial Physics*, *3*(4), 200–211. http://www.sciencedirect.com/science/article/pii/002191695390101X

Nishino, M., Nozawa, S., & Holtet, J. A. (1998). Daytime ionospheric absorption features in the polar cap associated with poleward drifting F-region plasma patches. *Earth, Planets and Space*, *50*(2), 107–117. https://doi.org/10.1186/BF03352092

Ohtani, S., Wing, S., Merkin, V. G., & Higuchi, T. (2014). Solar cycle dependence of nightside field-aligned currents: Effects of dayside ionospheric conductivity on the solar wind-magnetosphere-ionosphere coupling. *Journal of Geophysical Research: Space Physics*, *119*(1), 322–334. https://doi.org/10.1002/2013JA019410

Papitashvili, V. O., Christiansen, F., & Neubert, T. (2002). A new model of field-aligned currents derived from high-precision satellite magnetic field data. *Geophysical Research Letters*, *29*(14), 28-1–28-4. https://doi.org/10.1029/2001GL014207

Pignalberi, A., Pezzopane, M., Tozzi, R., De Michelis, P., & Coco, I. (2016). Comparison between IRI and preliminary Swarm Langmuir probe measurements during the St. Patrick storm period. *Earth, Planets and Space*, *68*(1), 93. https://doi.org/10.1186/s40623-016-0466-5

Pirjola, R., Kauristie, K., Lappalainen, H., Viljanen, A., & Pulkkinen, A. (2005). Space weather risk. *Space Weather*, *3*(2), S02. https://doi.org/10.1029/2004SW000112

Poedjono, B., Beck, N., Buchanan, A., Borri, L., Maus, S., Finn, C. A., et al. (2013). Improved geomagnetic referencing in the arctic environment. *SPE Arctic and Extreme Environments Conference & Exhibition (SPE-166850-PP)*. Moscow, Russia: Society of Petroleum Engineers.

Prölss, G. W. (2006). Subauroral electron temperature enhancement in the nighttime ionosphere. *Annales Geophysicae*, *24*(7), 1871–1885. https://doi.org/10.5194/angeo-24-1871-2006

Pulkkinen, A., Amm, O., & Viljanen, A. (2003). Ionospheric equivalent current distributions determined with the method of spherical elementary current systems. *Journal of Geophysical Research*, *108*(A2), 1053. https://doi.org/10.1029/2001JA005085

Rasmussen, C. E., Schunk, R. W., & Wickwar, V. B. (1988). A photochemical equilibrium model for ionospheric conductivity. *Journal of Geophysical Research*, *93*(A9), 9831–9840. https://doi.org/10.1029/JA093iA09p09831

Rees, M. H. (1963). Auroral ionization and excitation by incident energetic electrons. *Planetary and Space Science*, *11*(10), 1209–1218. https://doi.org/10.1016/0032-0633(63)90252-6

Richmond, A. D. (1995). Ionospheric electrodynamics using magnetic apex coordinates. *Journal of Geomagnetism and Geoelectricity*, *47*(2), 191–212. https://doi.org/10.5636/jgg.47.191

Rishbeth, H. (1997). The ionospheric E-layer and F-layer dynamos—a tutorial review. *Journal of Atmospheric and Solar-Terrestrial Physics*, *59*(15), 1873–1880. https://doi.org/10.1016/S1364-6826(97)00005-9

Robinson, R., Tsunoda, R. T., Vickrey, J. F., & Guerin, L. (1985). Sources of F region ionization enhancements in the nighttime auroral zone. *Journal of Geophysical Research*, *90*(A8), 7533–7546. https://doi.org/10.1029/JA090iA08p07533

Robinson, R., Vondrak, R. R., & Potemra, T. A. (1985). Auroral zone conductivities within the field-aligned current sheets. *Journal of Geophysical Research*, *90*(A10), 9688–9696. https://doi.org/10.1029/JA090iA10p09688

Rush, C. (1989). Ionospheric mapping-an update of foF2 coefficients. *Telecommunication Journal*, *56*(3), 179–182.

Savitzky, A., & Golay, M. J. E. (1964). Smoothing and differentiation of data by simplified least squares procedures. *Analytical Chemistry*, *36*(8), 1627–1639. https://doi.org/10.1021/ac60214a047

Shubin, V. N., Karpachev, A. T., & Tsybulya, K. G. (2013). Global model of the F2 layer peak height for low solar activity based on GPS radio-occultation data. *Journal of Atmospheric and Solar-Terrestrial Physics*, *104*, 106–115. https://doi.org/10.1016/j.jastp.2013.08.024, 2013.

Singh, R. N. (1966). The effective electron collision frequency in the lower F region of the ionosphere. *Proceedings of the Physical Society*, *87*(2), 425–428. https://doi.org/10.1088/0370-1328/87/2/311

Song, P., Vasyliunas, V., & Ma, L. (2005). Solar wind-magnetosphere-ionosphere coupling: Neutral atmosphere effects on signal propagation. *Journal of Geophysical Research*, *110*(A9), 309. https://doi.org/10.1029/2005JA011139

Spiro, R. W., Reiff, P. H., & Maher, L. J., Jr. (1982). Precipitating electron energy flux and auroral zone conductances-An empirical model. *Journal of Geophysical Research*, *87*(A10), 8215–8227. https://doi.org/10.1029/JA087iA10p08215

Stolle, C., Liu, H., Truhlk, V., Lhr, H., & Richards, P. G. (2011). Solar flux variation of the electron temperature morning overshoot in the equatorial F region. *Journal of Geophysical Research*, *116*(A4), 308. https://doi.org/10.1029/2010JA016235

Stumpo, M., Consolini, G., Alberti, T., & Quattrociocchi, V. (2020). Measuring Information Coupling between the Solar Wind and the Magnetosphere–Ionosphere System. *Entropy*, *22*(3), 276. https://doi.org/10.3390/e22030276

Takeda, M., & Araki, T. (1985). Electric conductivity of the ionosphere and nocturnal currents. *Journal of Atmospheric and Terrestrial Physics*, *47*(6), 601–609. https://doi.org/10.1016/0021-9169(85)90043-1

Tarpley, J. D. (1970). The ionospheric wind dynamo—II. Solar tides. *Planetary and Space Science*, *18*(7), 1091–1103. https://doi.org/10.1016/0032-0633(70)90110-8

Truhlik, V., Bilitza, D., & Triskova, L. (2009). Latitudinal variation of the topside electron temperature at different levels of solar activity. *Advances in Space Research*, *44*(6), 693–700. https://doi.org/10.1016/j.asr.2009.04.029

Truhlik, V., Bilitza, D., & Triskova, L. (2012). A new global empirical model of the electron temperature with the inclusion of the solar activity variations for IRI. *Earth, Planets and Space*, *64*(6), 531–543. https://doi.org/10.5047/eps.2011.10.016

Truhlik, V., Tskov, L., Milauer, J., & Afonin, V. (2000). Global empirical model of electron temperature in the outer ionosphere for period of high solar activity based on data of three Intercosmos satellites. *Advances in Space Research*, *25*(1), 163–169. https://doi.org/10.1016/S0273-1177(99)00914-X

Vickrey, J. F., Rino, C. L., & Potemra, T. A. (1980). Chatanika/Triad observations of unstable ionization enhancements in the auroral F-region. *Geophysical Research Letters*, *7*(10), 789–792. https://doi.org/10.1029/GL007i010p00789

Vickrey, J. F., Vondrak, R. R., & Matthews, S. J. (1981). The diurnal and latitudinal variation of auroral zone ionospheric conductivity. *Journal of Geophysical Research*, *86*(A1), 65–75. https://doi.org/10.1029/JA086iA01p00065

Wang, H., Lhr, H., & Ma, S. Y. (2005). Solar zenith angle and merging electric field control of field-aligned currents: A statistical study of the Southern Hemisphere. *Journal of Geophysical Research*, *110*(A3), 306. https://doi.org/10.1029/2004JA010530

Weygand, J. M., Amm, O., Viljanen, A., Angelopoulos, V., Murr, D., Engebretson, M. J., et al. (2011). Application and validation of the spherical elementary currents systems technique for deriving ionospheric equivalent currents with the North American and Greenland ground magnetometer arrays. *Journal of Geophysical Research*, *116*(A3), 305. https://doi.org/10.1029/2010JA016177

Zmuda, A. J., & Armstrong, J. C. (1974). The diurnal flow pattern of field-aligned currents. *Journal of Geophysical Research*, *79*(31), 4611–4619. https://doi.org/10.1029/JA079i031p04611

Zmuda, A. J., Martin, J. H., & Heuring, F. T. (1966). Transverse magnetic disturbances at 1100 kilometers in the auroral region. *Journal of Geophysical Research*, *71*(21), 5033–5045. https://doi.org/10.1029/JZ071i021p05033